On the optoelectronic mechanisms ruling Ti hyperdoped Si photodiodes

Eric García-Hemme*, Daniel Caudevilla, Sari Algaidy, Francisco Pérez-Zenteno, Rodrigo García-Hernansanz, Javier Olea, David Pastor, Álvaro del Prado, Enrique San Andrés, Ignacio Mártil, Germán González-Díaz

Dpto. de Estructura de la Materia, Física Térmica y Electrónica, Univ. Complutense de Madrid, 28040 Madrid, Spain

*Corresponding author email: eric.garcia@ucm.es

Abstract:

This work deepens in the understanding of the optoelectronic mechanisms ruling hyperdoped-based photodevices and shows the potential of Ti hyperdoped-Si as a fully CMOS-compatible material for room-temperature infrared photodetection technologies. By the combination of ion implantation and laser-based methods we obtain ~20 nm thin hyperdoped single-crystal Si layers with a Ti concentration as high as $10^{20}\ cm^{-3}$. The Ti hyperdoped Si/p-Si photodiode shows a room temperature rectification factor at ±1 V of 509. Analysis of the temperature dependent current-voltage characteristics shows that the transport is dominated by two mechanisms: a tunnel mechanism at low bias and a recombination process in the space charge region at high bias. A room-temperature sub-bandgap external quantum efficiency (EQE) extending to 2.5 μm wavelength has been obtained. Temperature-dependent spectral photoresponse behaviour reveals an increase of the EQE as the temperature decreases, showing a low energy photoresponse edge at 0.45 eV and a high energy photoresponse edge at 0.67 eV. Temperature behaviour of the open circuit voltage correlates with the high energy photoresponse edge. A model is proposed to relate the optoelectronic mechanisms to sub-bandgap optical transitions involving an impurity-band. This model is supported by numerical semiconductor device simulations using the SCAPS software.

1.- Introduction

Silicon, the cornerstone of the information revolution, is the most widely used, economically and technologically developed semiconductor. Although its applications cover many aspects of our everyday life, at present Si-based photonic applications are limited to the visible and near-infrared spectral range due to its 1.12 eV indirect bandgap (λ=1.1 µm). Extending Si photoresponse at room-temperature to the short-wavelength infrared (SWIR) range (1.4 to 3 µm, i.e., 0.89 to 0.41 eV) has the potential to revolutionize silicon-based optoelectronic devices. The introduction of a CMOS compatible process would enable the integration of optical and electronic functionality on a single chip [1]. Nowadays, several approaches are under intensive research to enhance Si SWIR photoresponse, such as the integration of III-V compound semiconductors with silicon [2,3], photodetectors based on SiGe alloys [4,5] or HgCdTe/Si heterostructures [6]. Despite their high performances, these devices suffer from several drawbacks: they are based on non-abundant or contaminant materials, they usually require cryogenic temperatures to operate, and they are hardly integrated into the very mature Si-CMOS fabrication routes, adding considerable cost and complexity to photonic circuit manufacturing.

An alternative path to increase the Si SWIR photoresponse that would avoid the hybrid integration of Si technology with unconventional materials is the direct modification of its electronic band structure. From this perspective it is possible to find interesting approaches. One is the use of a laser-crystallization process to induce an anisotropic tensile stress in silicon optical fibres. This way the bandgap can be reduced from 1.11 eV to 0.59 eV [7]. Unfortunately, the fibre structure hinders its incorporation into planar imaging arrays. A different method, that has attracted recently great attention [8], is the extrinsic sub-bandgap photoresponse obtained from the incorporation of deep-level impurities at concentrations far above their equilibrium values. Single-crystalline silicon layers with transition metal (Ti, V, Au, Ag) or chalcogen (S, Se, Te) at concentrations above 10^{19} cm^{-3} have been obtained by means of ion implantation and sub-second annealing techniques (in a process denominated as supersaturation or hyperdoping). We have shown that silicon hyperdoped with Ti [9,10] or V [11] presents outstanding properties such as a sub-bandgap optical absorption coefficient in the 10^4 cm^{-1} range [12] or a photoconductive response extended down to 0.2 eV (6.2 µm) at cryogenic temperatures [13]. Gold hyperdoped [14] [15] or silver hyperdoped [16] silicon photodiodes have proven a similar sub-bandgap photoresponse and fast response at room temperature. Silicon hyperdoped with S [17], Se [18] or Te [19] by ion implantation and subsequently Pulsed Laser Melted (PLM) or Flash Lamp Annealed (FLA) [20] [21] have also shown an extended infrared photoresponse [22] with high responsivities, and high specific detectivity values [23]. Unfortunately, competitive commercial devices have not yet been obtained. The main cause is the low sub-bandgap EQE obtained, which seems to be limited in all the current developed technologies to 0.01 % at the strategic 1450 nm wavelength. To overcome this disadvantage, it is necessary to explore and increase our understanding of the optoelectronic mechanisms ruling these technologies.

The nature and origin of these unusual sub-bandgap optical properties is still not well understood. The most accepted explanation is the formation of an impurity-band arising from the impurity deep-levels. In other words, given a critical impurity concentration, the localized electronic wavefunctions from the impurities would overlap, producing a delocalization transition and forming a continuum of allowed states within the bandgap of the host material. This critical concentration, also known as Luque’s limit, has been theoretically calculated to be approximately 6×10^{19} cm^{-3} for a generic deep-level impurity in Si [24], and experimentally confirmed for impurity concentrations in the order of 10^{20} cm^{-3} in the Ti, [25,26] V, [11] S, [27] and Se [28] hyperdoped-Si materials. Under this scenario, sub-bandgap optical transitions would be possible through the promotion of charge carriers involving the impurity band.

For the case of transition metals in Si, the technological challenge to obtain hyperdoped materials is particularly complex [29,30]. A lateral segregation effect of the metallic impurities appears when a combination of high implantation doses (usually higher than 5×10^{15} cm^{-2}) [31] and ns-laser annealing techniques is used. This segregation process, known as cellular-breakdown [32,33], might hinder the interpretation of the optoelectronic properties. However, at certain process conditions, it is indeed possible to obtain concentrations of transition metals above Luque's limit with a homogeneous distribution in the Si matrix and high crystalline quality. We have shown these results in previous works for the implantation of V [11] and Ti [34] at 32 keV with doses of 10^{15} cm^{-2} and the subsequent use of a KrF excimer laser (248 nm) with a 20 ns pulse duration at ~1 Jcm^{-2}.

To the best of our knowledge, the works published so far are focused on the proof of concept of the sub-bandgap photodetection. An in-depth analysis of the photogeneration nature, its temperature dynamics and the transport mechanism through the junction is required to identify possible weaknesses or limiting factors, as well as strengths and accordingly modify the manufacturing routes, aiming at the improvement of the photodiode characteristics.

This work studies the physical and electrical characteristics of a Ti hyperdoped-Si/p-Si junction photodiode. The Ti concentration depth profile is analysed and correlated with the microstructural information and crystalline quality. The room-temperature illumination and temperature-dependent dark current-voltage curves are presented and discussed. Si sub-bandgap External Quantum Efficiency (EQE) measurements are analysed up to 3.5 µm wavelength and its temperature behaviour is studied from 300 K to 140 K. Numerical semiconductor device simulations based on the SCAPS software [35] were performed and analysed and a model to explain the temperature dynamics involving the presence of an impurity band is proposed.

2.- METHODS

2.1.- Si-Hyperdoped Manufacturing:

The Ti hyperdoped-Si layer was obtained by means of ion implantation and pulsed laser melting processes on square-shaped samples 1×1 cm^2 in size of p-type (100) Si with a thickness of 300 µm ($\rho\sim$150-300 Ωcm at room temperature). Implantations were performed at 32 keV with $^{48}Ti^+$ ions (7° tilt angle) with a total dose of 2×10^{15} cm^{-2}. To recover the crystallinity of the amorphized surface layer we performed a 20 ns single-shot pulsed laser melting at 1 Jcm^{-2} with a KrF excimer laser (248 nm) at IPG Photonics (20 ns duration full width at half maximum). During the pulsed laser melting process, the implanted amorphous layer is melted. Afterwards, the underlying non-melted crystalline Si substrate acts as a crystalline seed and solidification occurs from this point towards the surface of the implanted layer. This solidification process occurs at high speed (1-10 m s^{-1}) [36], producing the incorporation of the implanted atoms at concentrations above the solid solubility limit.

2.2.- Microstructural Analysis

To analyse the resulting Ti hyperdoped-Si layer depth-profile, time-of-flight secondary ion mass spectrometry (ToF-SIMS) measurements were carried out in a ToF-SIMS V model manufactured by ION-TOF, with a 25 keV pulsed Bi3+ beam at 45° incidence. A 10.5 kV voltage was used to extract the secondary ions and their time of flight from the sample to the detector was measured with a reflection mass spectrometer. Measurements were performed under the dual beam configuration, allowing us to resolve depth profiles as steep as 1 nm/decade [37].

The crystalline quality was analysed by cross-sectional transmission electron microscopy (TEM) images. The pictures were taken with a Jeol JEM 3000F microscope operated at an accelerating voltage of 300 kV. Atomic number contrast images were recorded in the high-angle annular dark-field scanning transmission electron microscopy (HAADF-STEM) mode. For qualitative chemical analysis, energy-dispersive X-ray spectroscopy (EDX) measurements were done with an OXFORD INCA system attached to the JEM 3000F microscope.

2.3.- Photodiodes Manufacturing

Photodiodes were manufactured to characterize the Ti hyperdoped-Si/p-Si optoelectronic properties. To assure an ohmic back-side contact we performed an ion implantation with boron ($^{11}B^{+}$) at 7° tilt angle and 35 keV with a dose of 10^{15} cm^{-2}. Subsequently, a Rapid Thermal Annealing (RTA) in a forming gas atmosphere at 900 °C for 20 seconds was made to electrically activate the boron implantation. The RTA process was performed prior to the front-side Ti ion implantation and PLM to avoid the thermal instability issue of the Ti hyperdoped-Si material[47]. The back side electrode contact was obtained by evaporating 50 nm Ti + 100 nm Al on the whole back surface but masking sample edges to reduce possible parasitic electrical conduction through the device rim. A 0.068 cm^2 comb-shaped contact with 9 fingers (dimensions of each finger are 200 µm × 3830 µm, with 200 µm of separation between fingers) was deposited on the top of the Ti hyperdoped-Si layer. This contact was defined by lift-off of an e-beam evaporated 50 nm Ti + 100 nm Al metallic layer. Fig. 1 presents a schematic of the device geometry (dimensions not at scale) from a top view (left) and from a cross-section view (right).

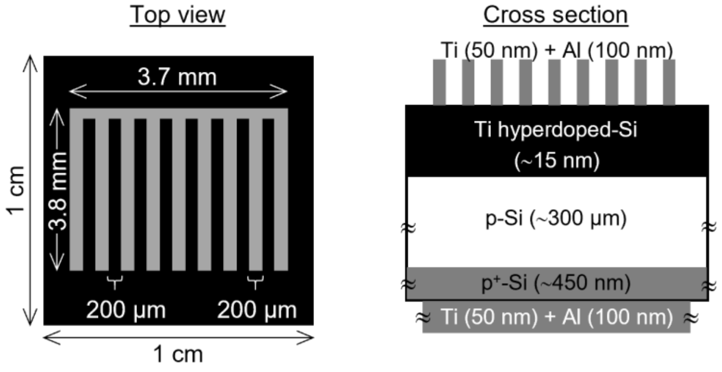

Figure 1: Top and cross section schematic views of the photodiode geometry (dimensions not at scale).

2.4.- Optoelectronic Characterization

An Everbeing probe station together with a Keythley 2636A SMU were used to perform the I-V measurements at room temperature. To test the photovoltaic effect of the photodiode we used an uncalibrated low intensity fluorescent lamp (Motic 2401). Samples were biased from −1 to 1 V with respect to the back electrode. For temperature-dependent measurements, samples were placed inside a helium closed-cycle Janis cryostat with a ZnSe window and a Pfeiffer Hi-Cube vacuum pump was used to avoid moisture condensation at low temperatures (these measurements were performed from

300 K to 140 K). For spectral EQE measurements the samples were illuminated in the 1 µm – 3.5 µm range using a TMc300 Bentham monochromator with a Globar (SiC) bar as infrared source. Light intensity was calibrated using a Bentham pyrometric detector. Measurements were carried out chopping the light beam at 87 Hz and the AC component of the generated short-circuit photocurrent was obtained with a SR830 digital signal processing lock-in amplifier, manufactured by Stanford Research Systems (California).

3.- Results:

3.1.- Structural properties:

Figure 2 presents the microstructural and compositional information of the Ti hyperdoped-Si material. For comparison purposes all the different figures are presented using the same scale. Fig. 2 a) shows the Ti depth profile obtained after the ion implantation and pulsed laser melting processes measured by Time of Flight-Secondary Ion Mass Spectrometry (ToF-SIMS). As a reference, the theoretical concentration limit needed for the appearance of an impurity band (Luque's limit) as well as the 1 atomic % of Ti in Si (5×10^{20} cm^{-3}) are highlighted. A Ti concentration far above the maximum solid solubility limit in Si (2×10^{14} cm^{-3}) [38] has been obtained in the Ti hyperdoped-Si layer. Specifically, Ti concentrations higher than the 1 atomic % were achieved in a layer of ~10 nm thick, while the thickness of the layer with a Ti concentration high enough to produce an impurity band (Luque's limit) is ~15 nm.

Fig. 2 b) shows a representative high-angle annular dark-field scanning transmission electron microscopy (HAADF STEM) micrograph obtained in the Si [001] axis. Brighter contrast corresponds to elements with a higher atomic number (Z-contrast image). A brighter layer is observed at a depth in agreement with the largest Ti concentration peak observed in the ToF-SIMS depth profile (~3 nm). This agrees with Ti having a higher atomic number than Si. Beyond this region, the brightness gradually decreases down to a depth of ~10 nm, where the brightest Ti signal (Z= 22) disappears submerged under the Si signal (Z= 14). At this depth, the corresponding Ti concentration reaches the 1 atomic %, which corresponds to the detection limit of the HAADF STEM technique. This gradual decrease of the brightness agrees with the gradual decrease of the Ti-concentration in the depth-profile shown in Fig. 2 a). High-resolution Transmission Electron Microscopy (TEM) image shown in Fig. 2 c) shows that the entire Ti hyperdoped-Si layer is monocrystalline, without the presence of any extended defects, secondary phases or cellular breakdown [33]. Finally, Fig. 2 d) presents the energy-dispersive X-ray spectroscopy (EDXS) map of the elements for the indicated region (red corresponds to Si, blue to Ti). EDXS detection limit is also ∼ 1 atomic %. According to the compositional map, there is a laterally uniform Ti distribution of ∼ 7 nm depth (Ti concentration higher than 1 atomic %) within the recrystallized Si layer. Since four different structural characterization techniques agree on the information given (within the sensitivities of each one) we can rule out the possibility of artifacts arising from a particular technique. Thus, Figure 2 shows a complete structural study which confirms that it is possible to obtain Ti homogeneously distributed in the Si matrix at concentrations higher than the Luque's limit.

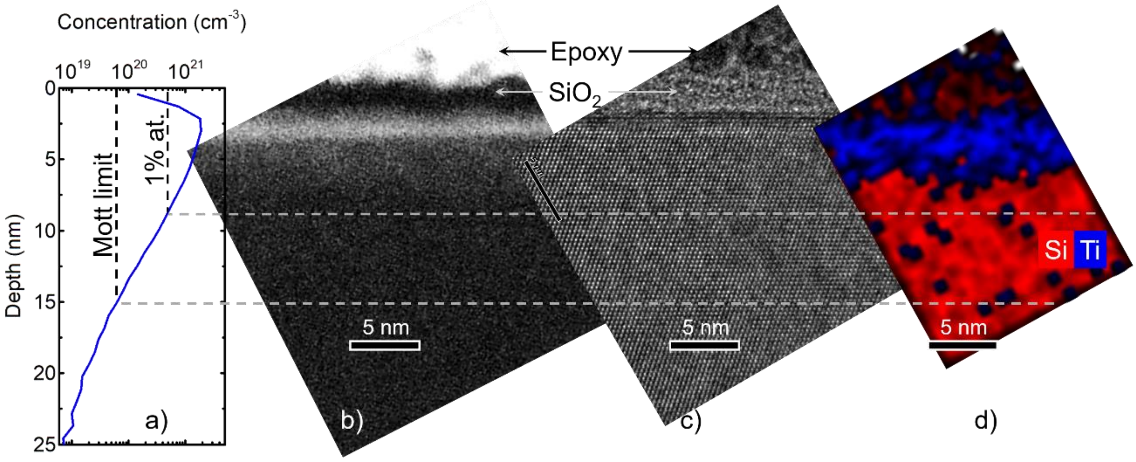

Figure 2: Microstructural and compositional analysis of the Ti hyperdoped-Si material. a) ToF-SIMS measurements showing the Ti concentration depth profile. 1 atomic % concentration and theoretical concentration to obtain an impurity band are marked as references. b) Atomic number contrast image recorded in HAADF-STEM mode. Brighter contrast observed near the surface corresponds to elements with a higher atomic number (Ti) with respect to the darker contrast obtained in the substrate (Si). c) High-resolution TEM image confirms the monocrystalline structure of the Ti hyperdoped-Si layer. d) Qualitative chemical map obtained from EDXS measurements indicating Si (red) and Ti (blue) presence.

3.2.- Electrical Properties:

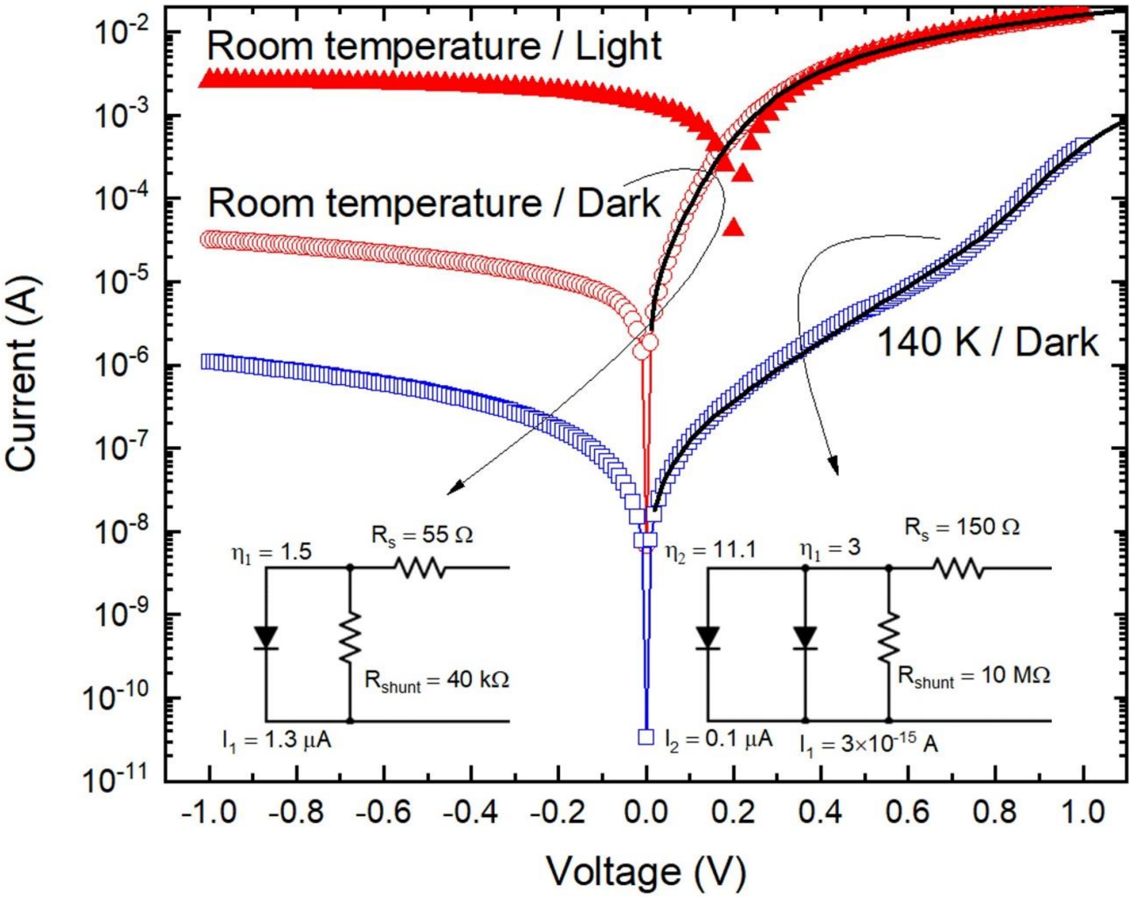

Figure 3: Room-temperature dark and under illumination current-voltage characteristics of the Ti hyperdoped-Si/p-Si photodiode. Dark IV curve at 140 K is also shown. Forward current bias is obtained when positive voltage is applied to the p-Si substrate. Black line shows the fit to the one-diode model and two-diodes model for the direct IV curve under dark conditions. The equivalent circuit used to fit the curve is shown together with the results of the fitting parameters.

To study the carrier transport properties, a prototype Ti hyperdoped-Si photodiode was manufactured. In junction devices, properties such as barriers due to band offsets or the presence of interface and bulk states will produce different carrier transport mechanisms. The dominance of one mechanism over the others depends on the bias region and/or temperature of operation. To study these transport processes, I-V curves, both in dark and under low illumination conditions are shown in Fig. 3 at room-temperature. An I-V curve in dark at 140 K is also shown. The device exhibits rectifying behaviour at both temperatures. Forward voltage corresponds to positive bias applied to the backside (p-Si substrate). The ratio of direct/reverse current at ±1 V is 509 at room-temperature and 390 at 140 K. To test the photovoltaic effect of the photodiode we used an uncalibrated low intensity fluorescent lamp (Motic 2401). A ~100 factor increases of the reverse current together with an open circuit voltage of 0.2 V were measured. Regarding the dark I-V curves, we observed two different regimes of transport as a function of temperature. At 300 K, the functional form of the forward current can be described by a general single-diode expression (continuous black line). However, at 140 K the shape of the I-V curve changes, and a change of slope appears at low bias. We fitted the low temperature experimental data to a two-diodes in parallel model (continuous black line). The expressions of these models are:

$$I = I_{D1} + I_{D2} + I_{SHUNT}$$

$$I = I_1\left[e^{\frac{q(V-IR_S)}{\eta_1 kT}} - 1\right] + I_2\left[e^{\frac{q(V-IR_S)}{\eta_2 kT}} - 1\right] + \frac{V-IR_S}{R_{Shunt}} \quad (1)$$

For the single-diode model we just used $I = I_{D1} + I_{SHUNT}$. In this expression, I_{D1} and I_{D2} correspond to the two main conduction mechanisms present in the photodiode. I_1, I_2 and η_1, η_2 are the saturation currents and ideality factors of each mechanism, whereas q is the electron charge, T the temperature, and k the Boltzmann constant. V and I are the measured voltage and current while R_S and R_{Shunt} are the series and parallel resistances, respectively. The equivalent circuits used to fit both curves are shown in Fig. 3 together with the results of the fitting parameters.

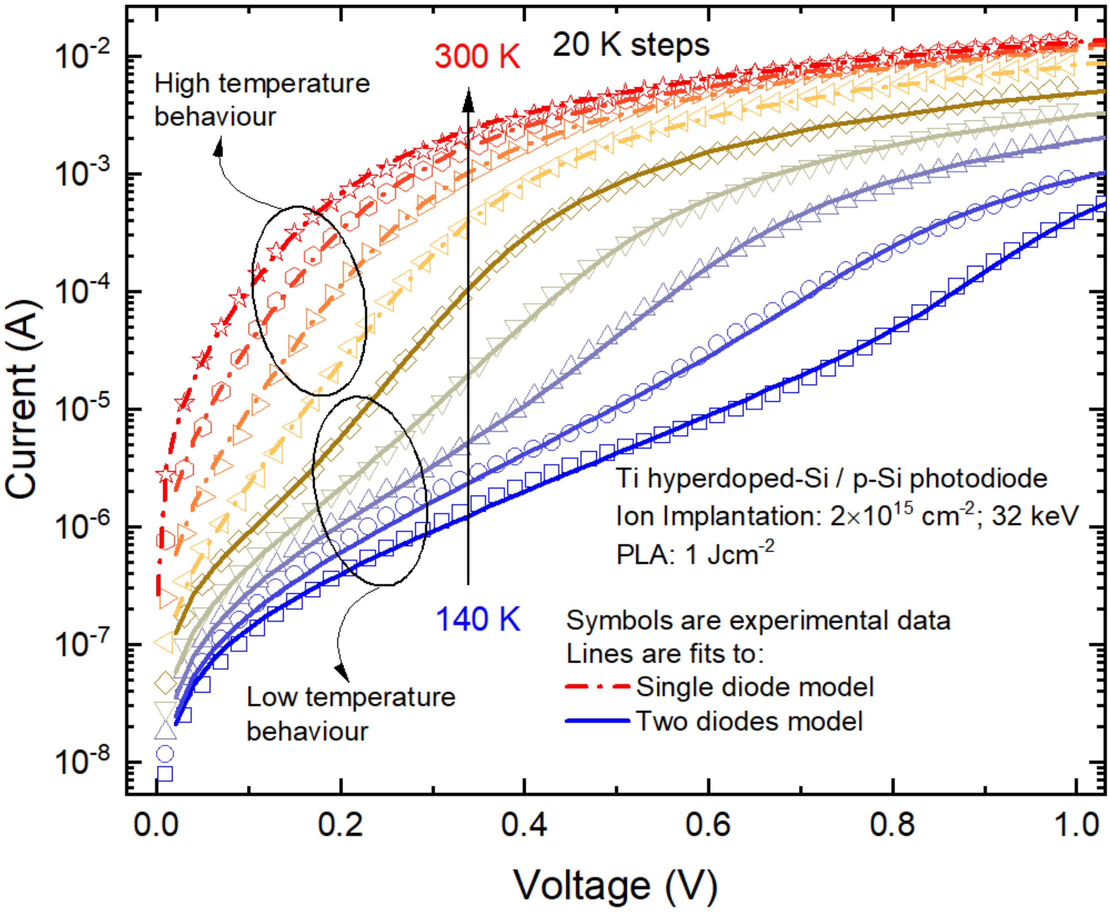

Figure 4: Temperature-dependent IV curve (solid symbols) together with fitting curves (solid and dashed lines). Dashed lines are used to identify the fitting curves obtained from the single diode model, while continuous lines represent the fitting to the two diodes model.

Fig. 4 presents the I-V curves measured from 140 K to 300 K in 20 K steps. Symbols are experimental data while continuous and discontinuous lines are fits to the two diodes model or single diode model, respectively. We observe that the single diode model stands from 300 K down to 240 K, indicating that a single transport mechanism is dominating. However, for temperatures lower than 220 K it was not possible to fit the measured I-V curves with the single diode model, and the two diodes model was used instead. This indicates that a second transport mechanism in parallel comes to the forefront, dominating the transport at low bias. From these fits we extracted the temperature dependence of the ideality factors, shown in Fig. 5 a), and of the saturation current, shown in Fig. 5 b). From this point, we will refer as the high temperature behaviour from 240 K to 300 K (where the single diode model holds), while the low temperature behaviour will correspond to the temperature range from 140 K to 220 K (two diodes model).

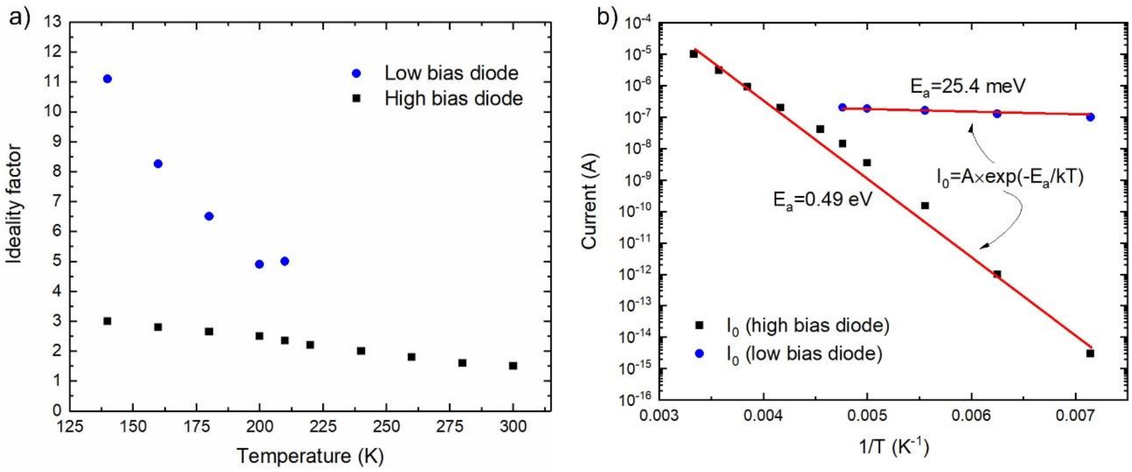

Figure 5: a) Temperature dependence of the ideality factors obtained from fitting the IV curves. b) Arrhenius plot of the saturation current values obtained from fitting the IV curves.

Regarding the temperature dependence of the ideality factors (Fig. 5 a), we can observe that the values obtained for the high bias diode present a slight temperature dependence, with an absolute increase from 1.5 to 3.0 as the temperature decreases from 300 K to 140 K. On the other hand, the low bias diode ideality factor presents a more intense temperature dependence, with an absolute increase from 5.0 to 11.1 as the temperature decreases from 220 K to 140 K.

The temperature dependence of the saturation current values is presented in an Arrhenius plot in Fig. 5 b). Both the low and the high bias diodes present an exponential activation of the saturation current values with the reverse temperature of the form:

$$I_0 = A \times exp\left(\frac{-E_a}{kT}\right) \qquad (2)$$

Where E_a represents the activation energy associated with the thermal dependence of the saturation current and A is a constant. In the case of the high bias diode, the exponential dependence holds for at least 10 orders of magnitude of the saturation current values, with an activation energy of 0.49 eV. On the other hand, the low bias diode presents a smaller temperature dependence, with an activation energy of 25.4 meV.

3.3.- Optoelectronic Properties:

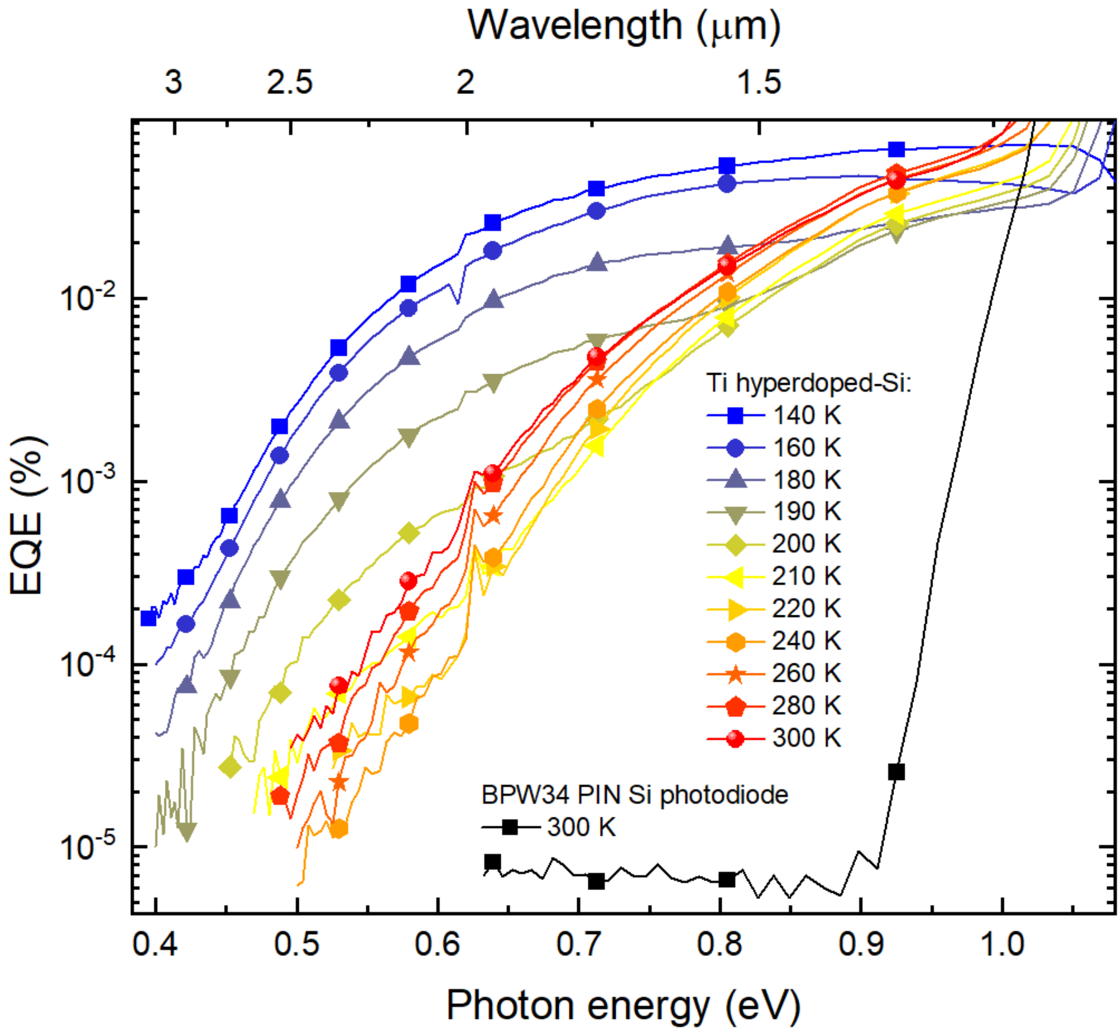

Figure 6: Temperature dependence of the spectral EQE for the Ti hyperdoped-Si/p-Si photodiode. Both temperature behaviours are indicated. As a reference, the spectral EQE of a standard Si PIN photodiode at room temperature is included.

To get insight into the mechanisms of the infrared photoresponse, Fig. 6 shows the temperature dependent spectral EQE curves obtained from the short-circuit photocurrent. EQE was analysed in the Si sub-bandgap region, i.e., from 1.0 µm to 3.5 µm (1.24 eV to 0.35 eV) and in the temperature range from room-temperature down to 140 K. For comparative purposes we present also the spectral EQE obtained from a commercial Si PIN photodiode (model BPW34) measured at room-temperature with the same setup.

The first thing to notice is that, as expected, the Si PIN photodiode shows an abrupt decrease of the EQE for photon energies lower than the 1.12 eV Si bandgap, due to the extinction of the Si band-to-band photogeneration. On the other hand, the Ti hyperdoped-

Si/p-Si photodiode presents a strong sub-bandgap photoresponse, several orders of magnitude higher than that of the Si PIN reference photodiode. Specifically, at room-temperature we measured an EQE of 2×10^{-4} (0.02 %) at the key telecommunication wavelength of 1.5 µm, 3 orders of magnitude higher than the noise floor.

Regarding the temperature dependence of the EQE we can identify two temperature ranges showing clearly different behaviours: from 300 K to 240 K (what we previously called the high temperature behaviour) the shape of the photoresponse is not altered while the signal level is slightly reduced as the temperature decreases. However, from 220 K down to 140 K (identified previously as the low temperature behaviour) the signal level increases abruptly and monotonically as the temperature decreases, showing a change in the shape with an additional broad photoresponse band spanning down to 0.4 eV.

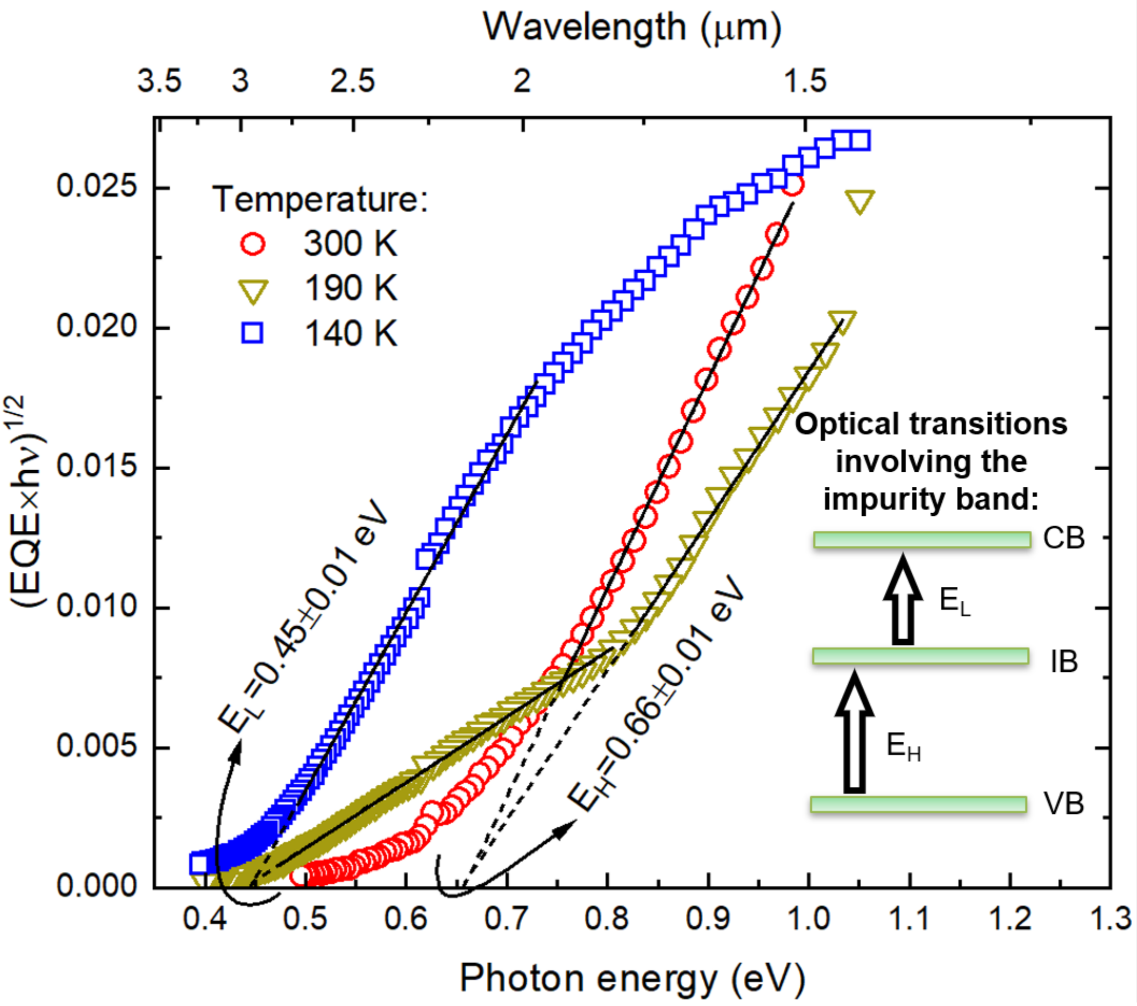

Figure 7: Spectral dependence of the magnitude $(EQE \times h\nu)^{\frac{1}{2}}$. Lines are fits to Eq. 3, which allows the identification of a low energy photoresponse edge (E_L) and a high energy photoresponse edge

(E_H). Inset represents a schematic of the sub-bandgap optical transitions involving the impurity band, where we have identified the low energy photoresponse edge (E_L) with the impurity band to conduction band transition and the high energy photoresponse edge (E_H) with the valence band to impurity band transition.

To further investigate the sub-bandgap optical transitions, in Fig. 7 we assume a direct correlation between the EQE and the absorption coefficient at energies corresponding to the optical transition edges. This representation allows us to identify a low energy photoresponse edge (E_L) appearing in the low temperature range and a high energy photoresponse edge (E_H) corresponding to the high temperature range. Based on previous experimental [39] and quantum calculations results [40], we associate both sub-bandgap photoresponse edges to optical transitions involving an impurity band, as shown in the inset of Fig. 7. This will be analysed deeply in the Discussion section. The direct correlation between the EQE and the absorption coefficient at photon energies corresponding to the optical transition edges allows us to perform a fit to equation 3 to estimate the E_L and E_H sub-bandgap energies transitions as [41]

$$EQE \times h\nu \propto (h\nu - E_i)^n \qquad (3)$$

where EQE is the external quantum efficiency, $h\nu$ is the photon energy, A is a constant, E_i is the sub-bandgap energy transition (E_L or E_H) and n would adopt the value of 0.5 for direct-bandgap optical transitions and 2 for indirect ones. We performed both fits to decide whether the direct or indirect transition applies. We found that data could be fitted better and in a wider energy range with the indirect bandgap approximation than with the direct bandgap approximation. Figure 7 represents the fittings of the data to Eq. 3 for the Ti hyperdoped-Si/p-Si photodiode at three representative temperatures: 300 K, 190 K and 140 K. 300 K and 140 K were chosen as examples of the high temperature and low temperature behaviours, respectively, while 190 K was chosen as representative of a transition temperature between both behaviours. For a representation of the behaviour at all temperatures see Fig. S1 and S2 in the supplementary material [42]. The energy gap obtained at 300 K is E_H=0.66 eV (~1.88 µm). At 190 K, together with the high-energy edge E_H, a low energy photoresponse edge appears with an energy gap of E_L=0.44 eV (~2.82 µm). Finally, at 140 K, the low energy photoresponse edge shows a higher signal with a similar energy gap of E_L=0.44 eV.

Note that the slight photocurrent measured below 0.65 eV at 300 K and below 0.45 eV at 140 K has not been considered for the fitting of E_H and E_L, respectively. This response just below the main sub-bandgap optical transitions energies (E_H and E_L) presents a weak signal with an unclear slope, characteristic of absorption by band tail states [43,44].

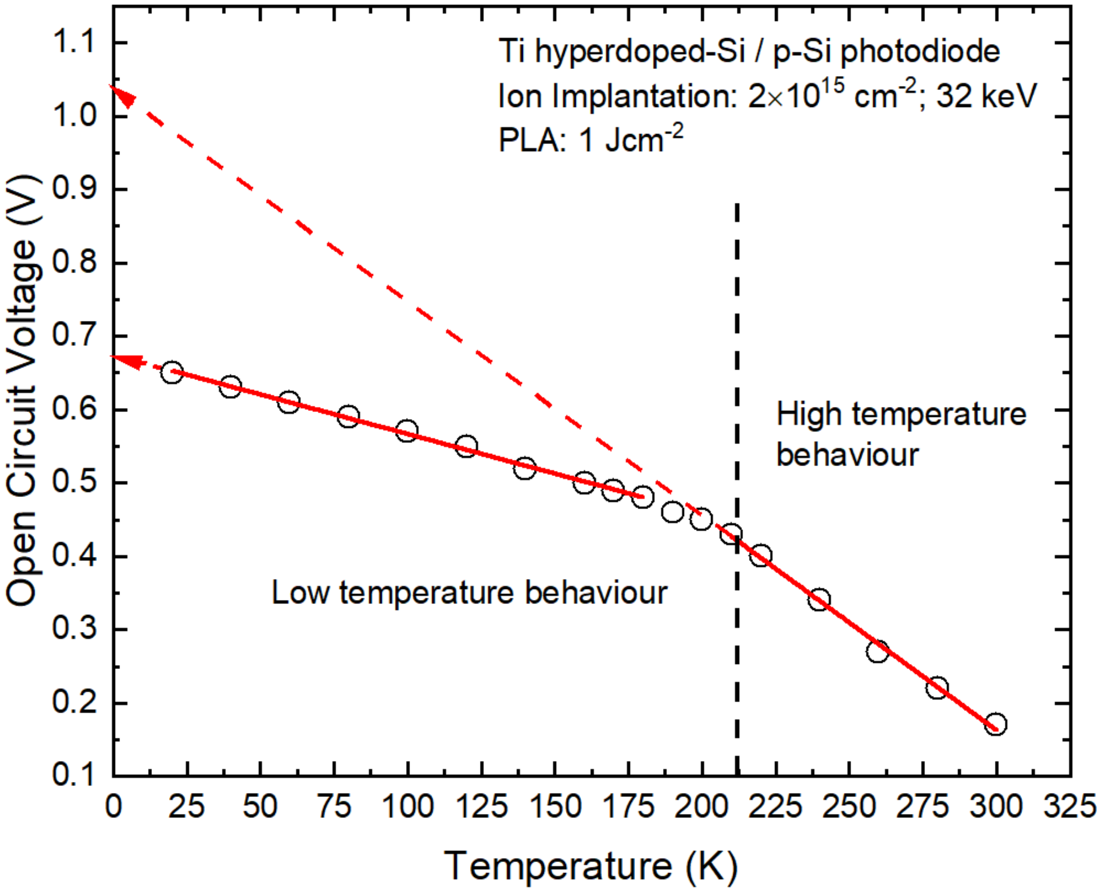

Figure 8: Temperature dependence of the open circuit voltage. Red lines are linear fittings used to obtain the 0 K extrapolated open circuit voltage. Both temperature regimes are identified

Figure 8 shows the temperature dependence of the open circuit voltage measured while the photodiode was illuminated with an uncalibrated low intensity halogen lamp. Again, we can observe two different linear trends as a function of temperature. In the high temperature range, from 240 K to 300 K, if we extrapolate to 0 K the V_{oc} we obtain 1.05 V. On the other hand, in the low temperature range, from 20 K to 220 K, the slope changes and the 0 K extrapolated V_{oc} equals 0.67 V. This value correlates well with the energy-equivalent value obtained for the high-energy edge E_H (Fig. 7). Later, in the discussion section we will analyse this correlation.

4.- Discussion

	Low temperature behaviour (140 K – 220 K)	**High temperature behaviour (240 K – 300 K)**
Electrical properties		
Ideality factor	High bias diode: 3.0-1.5	
	Low bias diode: 11.1-5.0	
Activation energy of the saturation current	High bias diode: 0.49 eV	
	Low bias diode: 25.4 meV	
Optoelectronic properties		
Photoresponse edges	E_H=0.67 eV	
	E_L=0.45 eV	
0 K extrapolated V_{OC}	0.67 V	1.05 V

Table I: Summary of the main results from the electrical and optoelectronic analysis for the Ti hyperdoped Si photodiode. These will be the key results for the discussion section.

In table I we have collected the key results from the electrical and optoelectronic analysis, to be discussed in this section. The analysis of the temperature dependent behaviour of the ideality factors $\left(\eta_{1,2}(t)\right)$ (Fig. 5 a) and the saturation current $\left(I_{1,2}(t)\right)$ (Fig. 5 b) will help us to identify the mechanisms controlling the transport across the junction. First, we analyse the high bias diode, which is present for all the temperatures measured. The ideality factor varies from 1.5 up to 3 as the temperature decreases. Following the Shockley diode theory, an ideality factor of 1 indicates that the transport is dominated by diffusion towards the neutral regions followed by recombination [45] while a value of 2 indicates that the transport is dominated by recombination processes in the depletion region. These recombination processes are assisted by traps situated within the bandgap [46]. Our calculated values, within experimental errors and fitting uncertainties, point to a transport mechanism dominated by recombination processes in the depletion region. Additionally, the activation energy of the saturation current obtained in Fig. 5 b) of 0.49 eV is close to the half of the silicon band gap (0.56 eV), which supports the conclusion that the transport mechanism is driven by recombination processes in the depletion region assisted by traps [46].

Secondly, we discuss the low bias diode, which becomes appreciable for temperatures below 220 K. The diode ideality factor presents a strong temperature dependence, showing an increase of its value as the temperature decreases, from 5.0 at 220 K up to 11.1 at 140 K. Such temperature-dependent ideality factor behaviour is commonly related to trap assisted tunnelling processes [47]. Additionally, its saturation current values present a small activation energy of 25.4 meV. Such small activation energy supports the transport being dominated by a trap assisted tunnelling process at low bias [48,49].

Next, we discuss the results derived from the temperature-dependent analysis of the spectral EQE and its relationship with the electronic transport mechanisms. It is noteworthy that the temperature of the appearance of the low energy photoresponse edge (E_L) coincides with the temperature at which the transport mechanism is dominated by a tunnelling process at low bias. Besides, the 0 K extrapolated $q \times V_{OC}$ energy for the low temperature behaviour (Fig. 8) coincides with the high energy photoresponse edge (E_H). To shed light on these apparently non-related phenomena, we performed numerical simulations based on the coupled Poisson and carrier-continuity equations by using the SCAPS software [35]. SCAPS simulates both thermal and optical processes considering deep-lying states within the host semiconductor bandgap. We propose that the deep-level states associated with the Ti atoms would form an impurity band within the Si bandgap. Then, we relate both energy photoresponse edges (E_L and E_H) with the sub-bandgap optical transitions involving an impurity band within the Si bandgap (Fig. 7 inset). Specifically, we relate E_L with IB-CB transitions while E_H is related with VB-IB transitions. This choice is based on previous quantum calculations results [40]. The impurity band is simulated as a Si material with a Gaussian continuous distribution of donor-like states located at 0.45 eV under the Si conduction band with a characteristic energy of 135 meV and a 10^{20} cm^{-3} total density of donor-like states. These chosen values to simulate the Gaussian distribution are based as well on previous results from quantum calculations [40].

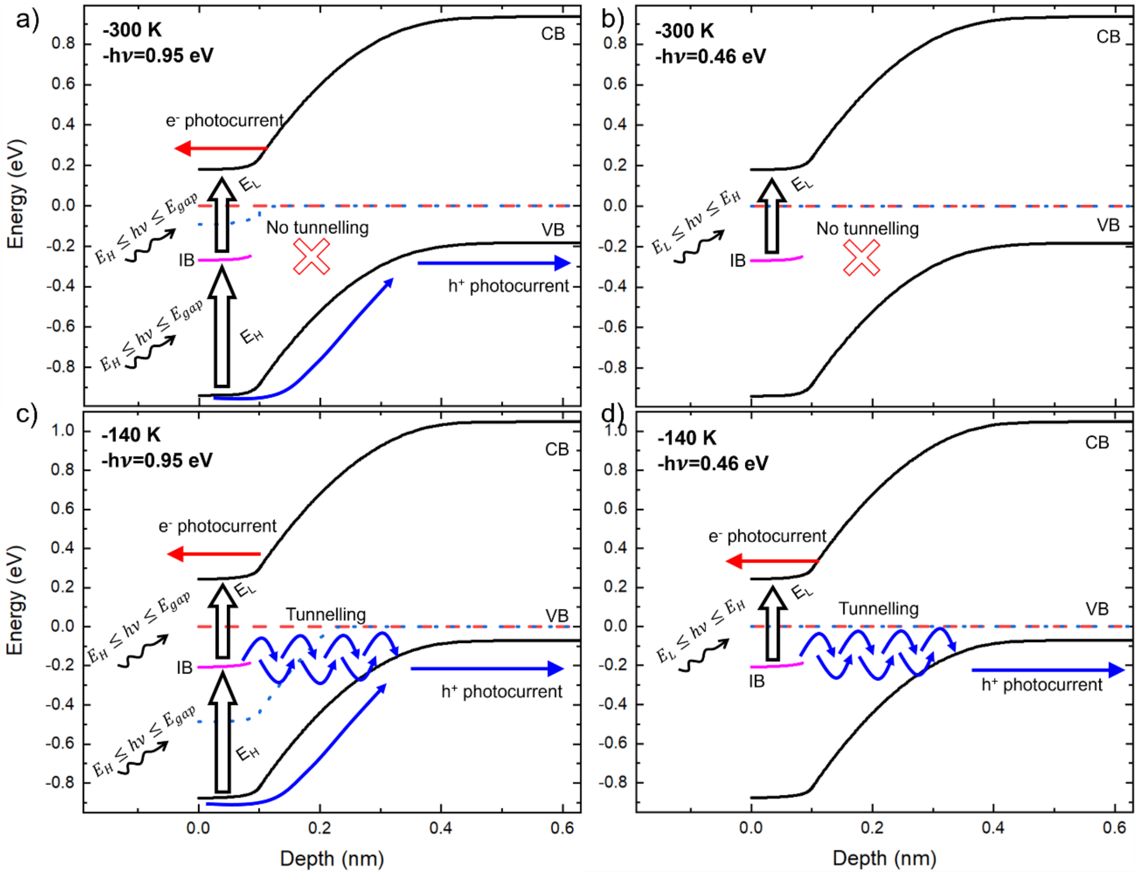

Figure 9: Simulated energy band diagrams together with schematics for the transport mechanisms and optical transitions for the structure Ti hyperdoped Si/p-Si substrate. Red dashed line represents the electron quasi-Fermi level (F_n) while blue dotted line corresponds to the hole quasi-Fermi level (F_p). Simulations were performed with the SCAPS software at short circuit condition, under a 100 mW/cm^2 monochromatic light. Simulated temperatures were chosen as representative of the high temperature behaviour in a) and b) (300 K), and of the low temperature behaviour in c) and d) (140 K). Monochromatic photon energies were chosen to allow only E_L sub-bandgap optical transition in b) and d) (hν=0.46 eV), or both sub-bandgap optical transitions, E_L and E_H in a) and c) for (hν=0.95 eV).

The simulated band diagrams at short circuit condition are shown in Fig. 9. Simulated temperatures were chosen as representative of the high temperature behaviour in a) and b) (300 K), and of the low temperature behaviour in c) and d) (140 K). Monochromatic photon energies were chosen to allow only E_L sub-bandgap optical transition in b) and d) (hν=0.46 eV), or both sub-bandgap optical transitions, E_L and E_H in a) and c) for (hν=0.95 eV)

In the high temperature range, we previously observed in Fig. 6 that a significant photoresponse was obtained when the photon energy was equal or higher than the VB-IB distance (E_H). Under this light condition, both sub-bandgap transitions VB - IB and

IB - CB are allowed, promoting free e^- - h^+ pairs and thus producing a net photocurrent as depicted in Fig. 9 a). The reason why in the high temperature range we were not able to probe optical transitions for photon energies $E_L<h\nu<E_H$ could be related with the electrical disconnection of the IB with the p-Si substrate valence band (Fig. 9 b). To measure a photogenerated current produced only by IB - CB optical transitions (E_L), photogenerated holes in the impurity band should be able to travel to the valence band of the p-Si substrate to close the electronic circuit with photogenerated electrons in the conduction band of the Ti hyperdoped Si layer.

However, in the low temperature range we deduced the existence of a tunnelling current from the analysis of Fig. 5. This coincides with the temperature range at which we observed an abrupt increase of the photoresponse for photon energies equal or higher than E_L. We propose that photons with energy $E_L< h\nu < E_H$ create e^--h^+ pairs in the conduction band and impurity band, respectively. Photogenerated holes in the impurity band can now travel to the substrate valence band through the tunnelling mechanism as it is depicted in Fig. 9 d). This way, it is possible to probe a net photocurrent related to the E_L optical transition.

From the simulations there are two facts that support the appearance of the tunnelling current as the temperature decreases. First, the distance between the edge of the impurity band and the p-Si substrate valence band reduces from 208 nm at 300 K to 167 nm at 140 K, therefore increasing the tunnelling probability. Second, the energetic position of the top of the p-Si substrate valence band with respect to the impurity band increases from 124 meV at 300 K to 313 meV at 140 K. Therefore, a higher density of states of the p-Si valence band is aligned with the impurity band, increasing the hole tunnelling probability.

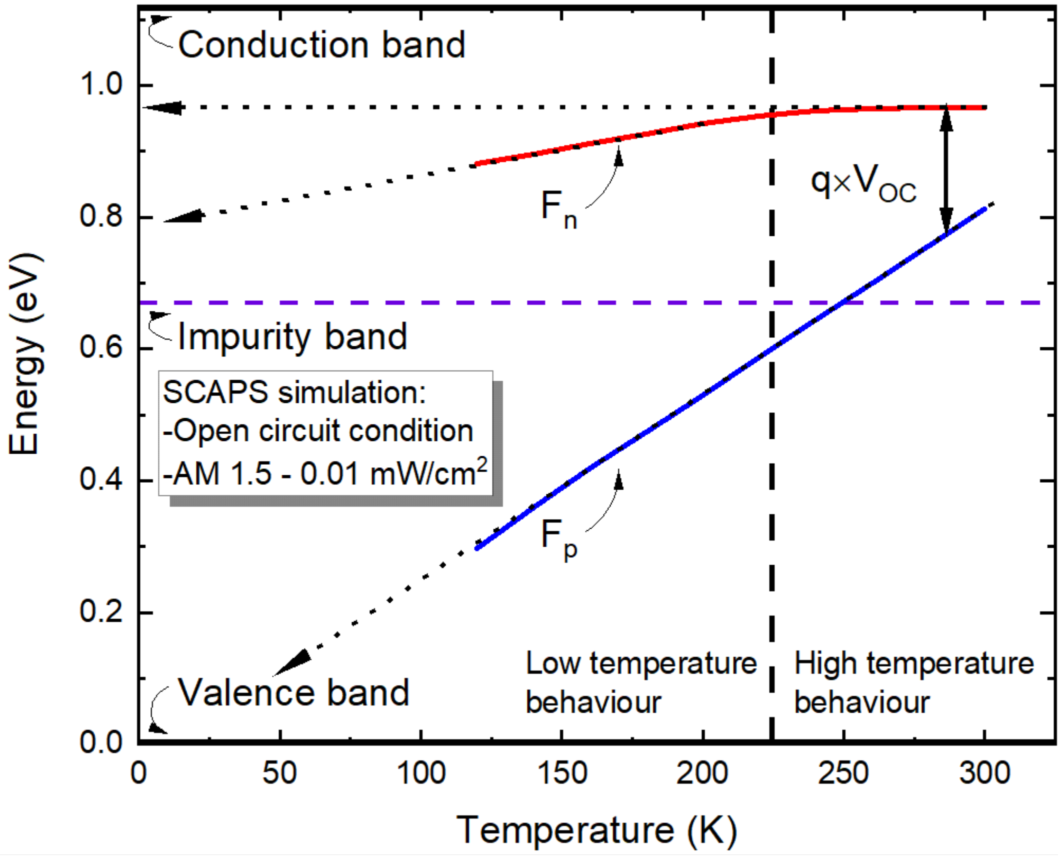

Figure 10: Simulated temperature dependence for the electron quasi-Fermi level (F_n) and for the hole quasi-Fermi level (F_p) in the Ti hyperdoped Si layer using the SCAPS software. Simulations are performed for the open circuit condition and using a reference AM 1.5 spectrum and under an irradiance of 0.01 mW/cm^2 to simulate the experimental conditions. The Ti hyperdoped Si conduction band (top of the figure and valence band (bottom of the figure) are also indicated. As a reference, the impurity band energetic position derived from the analysis of Fig. 7 is also presented. Arrows indicate the 0 K extrapolated F_n and F_p energetic position.

Recalling the temperature behaviour of the open circuit voltage (Fig. 8), we observed two different trends as a function of the temperature: in the high temperature range, the 0 K extrapolated $q \times V_{OC}$ energy corresponds roughly to the Si band gap energy (1.05 eV) while the 0 K extrapolated $q \times V_{OC}$ energy for the low temperature range corresponds to 0.67 eV, a value close to the E_H optical transition (VB-IB). In the Shockley-Queisser theory, the quasi-Fermi level splitting and the V_{OC} are two interchangeable quantities which are considered as equal [50,51]. To understand this result, in Fig. 10 we show the temperature-dependent energy of the electron quasi-Fermi level (F_n) and of the hole quasi-Fermi level (F_p) in the Ti hyperdoped Si layer, obtained from the simulation of the band diagrams at the open circuit condition. Simulations were performed in the temperature range from 300 K to 120 K (for temperatures below 120 K the simulation failed to converge). The temperature behaviour of F_p is as expected, i.e., F_p approaches the VB as the temperature decreases. This is because the hole concentration, which is due to the light generation, is approximately constant as the temperature decreases. Regarding F_n, it does not change in the high temperature range, while for the low temperature behaviour F_n approaches the top of the IB. This is the expected behaviour of a compensated semiconductor [52]. In the hyperdoped layer we have a high concentration of Ti atoms that could be acting as deep donor levels, being compensated by the background acceptor concentration. The difference between the background acceptor concentration ($N_A=10^{15}$ cm^{-3}) and the Ti deep donor levels concentration (~10^{20} cm^{-3}) could appear extremely high to talk of a compensation process. However, despite this high concentration differences, the low temperature behaviour of F_n is ruled by the compensation process for the case of a deep donor level [52].

The behaviour of F_n and F_p shown in Fig. 10 would explain the V_{OC} temperature dependence observed in Fig. 8:

1. In the high temperature range, the 0 K extrapolated F_n intersects an energy of ≈1 eV, while the 0 K extrapolated F_p will intersect an energy close to 0 eV, resulting in a quasi-Fermi level splitting of ≈1 eV, i.e., an V_{OC} of ≈1 V. This supports the 0 K extrapolated V_{OC} observed experimentally in Fig. 8 for the high temperature behaviour.
2. In the low temperature range, the 0 K extrapolated F_n changes its tendency and intersect an energy of ≈0.79 eV, while the 0 K extrapolated F_p will continue to intersect an energy close to 0 eV, resulting in a quasi-Fermi level splitting of ≈0.79 eV, i.e., an V_{OC} of ≈0.79 V. In this case, the extrapolated value obtained from the simulation is approximately 100 mV higher than the 0 K extrapolated V_{OC} observed experimentally in Fig. 8 for the low temperature range. This discrepancy could be explained considering that we simulated the IB as a Gaussian continuous distribution of donor-like states with a characteristic energy of 125 meV centred at 0.67 eV. In any case, we consider the key point to be the temperature-dependence change of F_n from the high temperature range to the low temperature range, and its correlation with the temperature behaviour of the V_{OC}.

As a result, the temperature behaviour of the V_{OC} could be used as a tool to identify the energetic position of the impurity band. This is supported by the fact that the impurity band energetic position given by the analysis of the V_{OC} temperature behaviour coincides with the E_H optical transition (VB-IB) identified in the analysis of Fig. 7.

One final key point remains to be discussed from the analysis of Fig. 10. The thermal behaviour of F_n shows the same temperature regimes as the transport mechanisms analysed in Fig. 4 and 5. These apparently unconnected phenomena could be in fact intimately related. From the transport mechanisms analysis, we concluded that at high bias the transport is dominated by recombination processes in the space charge region. These recombination processes are mediated by the presence of trap states in the space charge region. The presence of these traps supports the trap assisted tunnelling processes between the impurity band and the substrate valence band discussed in the analysis of the transport mechanisms and represented in Fig. 9. However, the occupation state of these traps is critical for the probability of the tunnelling process. F_n describes not only the occupation of states of the conduction band, but also of the traps present in the space charge region. When F_n decreases its energetic position as the temperature decreases, it implies a higher density of empty traps, therefore increasing the trap assisted tunnelling probability [48]. The presence of traps in the space charge region can be explained by process-induced defects [53]. Both, ion implantation and PLM produce different kind of point defects in Si. For instance, PLM-induced vacancies are measurable even at up to a micrometer beyond the laser processed Si surface [54]. Ion implantation also produces a large number of highly mobile interstitials residing beyond the end-of-range (EOR) [55].

It is interesting to note that the sum $E_H + E_L$ =1.1 eV, is a value close to the Si bandgap, supporting the proposed model of a sub-bandgap photoresponse mediated by an impurity band. Following this reasoning, the Ti impurity band would be located at $E_C - E_{IB} = 0.45$ eV. This result agrees well with the quantum calculations based on density-functional theory made by K. Sánchez et al., [40] where they located the IB at 0.5 eV from the CB. In their work, Sánchez et al. calculate IB energetic positions as a function of different configurations and concentrations. The referenced value of 0.5 eV from the CB is the calculated value for the configuration Ti_iSi_{216}, a supercell of conventional Si_8 cubic unit cell of 3×3×3, with Ti atoms placed in interstitial positions. This configuration corresponds to the relaxed structure with the Ti concentration and Ti lattice position closer to the experiment [56]. The slight difference between the experimental (0.45 eV) and the calculated (0.5 eV) values could be related to the approximations needed during the quantum calculations to attempt to correct the Si bandgap and to the experimental uncertainty.

The indirect character of both sub-bandgap transitions E_L and E_H obtained in Fig. 7 could be related with previous results on the electronic transport in the impurity band. From previous works [57] we extracted the low temperature mobility of the impurity band in Ti hyperdoped Si layers to be extremely low (in the order of 0.1 $cm^2V^{-1}s^{-1}$), pointing to a band with a high effective mass, i.e., a flat band. With such flat band, it could be hard to clearly identify the minimums and maximums of the impurity band, and therefore, to clearly define a direct transition, making the indirect transitions between the impurity band and the CB or VB the most probable transition.

The proposed IB energetic position is close to some of the referenced values for the Ti donor level in Si such as Ec – 0.512 eV in Ref. [58], or Ec – 0.49 eV in Ref. [59] However it is important to note that the position of the impurity band is not necessarily related to the energetic position of the isolated deep level impurity [40].

Another feature which could be of great interest in these materials is the analysis of the Si band-edge (photons energies higher than 1.12 eV) and its temperature dependence. Due to the high density of impurity states, an electronic interaction with the Si conduction and/or valence band may take place. Such interaction could modify the Si bandgap, or even make the Si band-edge to evolve into the direct bandgap feature. This is in fact a distinguishing feature of highly mismatch alloys, a different and fruitfully strategy to obtain impurity band materials [60,61]. Unfortunately, this feature cannot be studied in the present work. Once we illuminate the photodiode with photon energies equal or higher than the Si bandgap, the underlying 300 microns Si substrate starts to contribute to the total photocurrent. Due to its higher thickness compared to the Ti hyperdoped Si layer thickness (20 nm), its contribution to the total photocurrent could masks any contribution from the Ti hyperdoped Si layer. For this reason, we have decided to focus our study on the sub-bandgap region.

One can argue that the observed sub-bandgap photoresponse could be due to a two-photon-absorption (TPA) process. However, it is known that a TPA process presents a quadratic dependence of the photogenerated photocurrent with the input optical power [62]. The linear sub-bandgap dependence observed in Fig. S3 of the supplementary material [42] discards a TPA process, supporting the previously discussed scenario of a single-photon absorption mediated by an impurity band.

The 0.02 % room-temperature EQE measured at the key telecommunication wavelength of 1.5 µm is among the present best technologies based on hyperdoped Si. Nevertheless, there is still plenty of room for improvements. In future works, to boost the overall sub-bandgap efficiency of the devices, we will focus on increasing the absorptance of the material. For that, the first step would be to thoroughly understand the optical properties of the hyperdoped materials. We will perform temperature-dependent transmission and reflectance experiments as an addition to the room-temperature results published in [12]. In parallel, we are exploring strategies such as developing a new technology to increase the thickness of the hyperdoped material or by incorporating an anti-reflection coating. Additionally, Meng-Ju Sher et. al., [63] showed that the lifetime in chalcogen-hyperdoped Si is in the ps-ns range. With such a short lifetime is key to develop charge carrier collection strategies, such as the application of intense electric fields, the incorporation of a passivating layer or the use of architectures such as pin photodiodes or gate-controlled phototransistors. Finally, in this work we have shown that a great increase of the photoresponse is obtained once the substrate valence band is accessible by tunnelling from the impurity band. Therefore, a strategy to increase the photoresponse of future devices will be to explore new device architectures to facilitate this electronic transport path.

5.- Conclusions

A Ti hyperdoped-Si/p-Si photodiode operating at room-temperature has been manufactured by means of a CMOS compatible route based on ion implantation and pulsed laser melting processes. A detailed structural and compositional characterization has revealed a single crystalline Ti hyperdoped-Si layer with Ti homogeneously distributed at concentrations as high as 1 atomic %. A clear rectification behaviour as well as a 0.2 V open circuit voltage was measured. Analysis of the electronic properties with variable temperatures has revealed two main transport mechanisms: a recombination in the space charge region at high bias and a tunnel transport mechanism appearing at low temperatures and low bias. By an in-depth characterization of the temperature dependent spectral EQE results, we reported a consistent explanation for the nature of the sub-bandgap photoresponse. The proposed mechanism considers the formation of an impurity band within the Si bandgap, which allows for sub-bandgap optical transitions. These optical transitions were determined to be $E_L=E_{CB}-E_{IB}=0.45$ eV and $E_H=E_{IB}-E_{VB}=0.67$ eV. Supported by numerical semiconductor simulations, we revealed that the contribution of the low energy photoresponse edge E_L to the total photocurrent is directly related to the tunnelling mechanism. Only when the substrate valence band is electrically connected with the impurity band it is possible to probe the E_L contribution to the photocurrent. Finally, the temperature dependence of the open circuit voltage could be used as a powerful tool to estimate the energetic position of the impurity band within the Si bandgap. We showed that the extrapolated 0 K open circuit voltage value is directly related with the temperature behaviour of the electron quasi-Fermi level (F_n), which tends to the top of the impurity band as the temperature tends to 0 K.

The 0.02 % EQE measured at the 1.5 µm key telecommunication wavelength is just the first step. A full optimization of this proof-of-concept device could boost the efficiency at 1.5 µm, making these hyperdoped-Si materials robust candidates for room-temperature CMOS compatible SWIR photodetectors.

ACKNOWLEDGEMENTS

Authors would like to acknowledge the technical and human support provided by Facility of Analysis and Characterization of Solids and Surfaces of SAIUEx (financed by UEX, Junta de Extremadura, MICINN, FEDER and FSE), as well as the CAI de Técnicas Físicas of the Universidad Complutense de Madrid for the ion implantation and rapid thermal annealing processes, and the ICTS Centro Nacional de Microscopía Electrónica for the microstructural measurements. We would like to thank Marc Burgelman for his helpful discussion about the use of SCAPS software. We would like to thank Sven Kayser from IONTOF GmbH (Germany) for his helpful discussion about the dual beam configuration and ion beam mixing artefact. This work was partially supported by the Project MADRID-PV2 (P2018/EMT-4308) funded by the Regional Government of Madrid with the support from FEDER Funds., by the Spanish MINECO (Ministerio de Economía y Competitividad) under grants TEC2017-84378-R, PID2020-116508RB-I00 and PID2020-117498RB-I00. Daniel Caudevilla would also acknowledge the grant PRE2018-083798, financed by MICINN and European Social Fund. The authors are also thankful for financial collaboration from the Mexican grants program CONACyT.

REFERENCES:

[1] A. Rogalski, *Infrared Detectors: Status and Trends*, Progress in Quantum Electronics.

[2] H. Wook Shin, S. J. Lee, D. G. Kim, M. H. Bae, J. Heo, K. J. Choi, W. J. Choi, J. W. Choe, and J. C. Shin, *Short-Wavelength Infrared Photodetector on Si Employing Strain-Induced Growth of Very Tall InAs Nanowire Arrays*, Sci. Rep. **5**, (2015).

[3] D. Liang, G. Roelkens, R. Baets, and J. E. Bowers, *Hybrid Integrated Platforms for Silicon Photonics*, Materials.

[4] J. Michel, J. Liu, and L. C. Kimerling, *High-Performance Ge-on-Si Photodetectors*, Nat. Photonics **4**, (2010).

[5] Y. Kang, H. D. Liu, M. Morse, M. J. Paniccia, M. Zadka, S. Litski, G. Sarid, A. Pauchard, Y. H. Kuo, H. W. Chen, W. S. Zaoui, J. E. Bowers, A. Beling, D. C. McIntosh, X. Zheng, and J. C. Campbell, *Monolithic Germanium/Silicon Avalanche Photodiodes with 340GHz Gain-Bandwidth Product*, Nat. Photonics **3**, 59 (2009).

[6] V. M. Bazovkin, S. A. Dvoretsky, A. A. Guzev, A. P. Kovchavtsev, D. V. Marin, V. G. Polovinkin, I. V. Sabinina, G. Y. Sidorov, A. V. Tsarenko, V. V. Vasil'Ev, V. S. Varavin, and M. V. Yakushev, *High Operating Temperature SWIR P+-n FPA Based on MBE-Grown HgCdTe/Si(0 1 3)*, Infrared Phys. Technol. **76**, (2016).

[7] N. Healy, S. Mailis, N. M. Bulgakova, P. J. A. Sazio, T. D. Day, J. R. Sparks, H. Y. Cheng, J. V. Badding, and A. C. Peacock, *Extreme Electronic Bandgap Modification in Laser-Crystallized Silicon Optical Fibres*, Nat. Mater. **13**, (2014).

[8] M. Wang and Y. Berencén, *Room-Temperature Infrared Photoresponse from Ion Beam–Hyperdoped Silicon*, Phys. Status Solidi Appl. Mater. Sci. **218**, (2021).

[9] E. García-Hemme, R. García-Hernansanz, J. Olea, D. Pastor, A. Del Prado, I. Mártil, and G. Gónzalez-Díaz, *Sub-Bandgap Spectral Photo-Response Analysis of Ti Supersaturated Si*, Appl. Phys. Lett. **101**, (2012).

[10] E. García-Hemme, R. García-Hernansanz, J. Olea, D. Pastor, A. Del Prado, I. Mártil, and G. González-Díaz, *Room-Temperature Operation of a Titanium Supersaturated Silicon-Based Infrared Photodetector*, Appl. Phys. Lett. **104**, (2014).

[11] E. García-Hemme, D. Montero, R. García-Hernansanz, J. Olea, I. Mártil, and G. González-Díaz, *Insulator-to-Metal Transition in Vanadium Supersaturated Silicon: Variable-Range Hopping and Kondo Effect Signatures*, J. Phys. D. Appl. Phys. **49**, (2016).

[12] J. Olea, A. Del Prado, D. Pastor, I. Mártil, and G. González-Díaz, *Sub-Bandgap Absorption in Ti Implanted Si over the Mott Limit*, J. Appl. Phys. **109**, (2011).

[13] E. García-Hemme, R. García-Hernansanz, J. Olea, D. Pastor, A. Del Prado, I. Mártil, and G. González-Díaz, *Far Infrared Photoconductivity in a Silicon Based Material: Vanadium Supersaturated Silicon*, Appl. Phys. Lett. **103**, (2013).

[14] J. P. Mailoa, A. J. Akey, C. B. Simmons, D. Hutchinson, J. Mathews, J. T. Sullivan, D. Recht, M. T. Winkler, J. S. Williams, J. M. Warrender, P. D. Persans, M. J. Aziz, and T. Buonassisi, *Room-Temperature Sub-Band Gap Optoelectronic Response of Hyperdoped Silicon*, Nat. Commun. **5**, (2014).

[15] S. Q. Lim, T.-K. Lew, P. K. Chow, J. M. Warrender, J. S. Williams, and B. C. Johnson, *Toward Understanding and Optimizing Au-Hyperdoped Si Infrared Photodetectors*, **8**, 61109 (2020).

[16] X. Qiu, X. Yu, S. Yuan, Y. Gao, X. Liu, Y. Xu, and D. Yang, *Trap Assisted Bulk Silicon Photodetector with High Photoconductive Gain, Low Noise, and Fast Response by Ag Hyperdoping*, Adv. Opt. Mater. **6**, (2018).

[17] A. J. Said, D. Recht, J. T. Sullivan, J. M. Warrender, T. Buonassisi, P. D. Persans, and M. J. Aziz, *Extended Infrared Photoresponse and Gain in Chalcogen-Supersaturated Silicon Photodiodes*, Appl. Phys. Lett. **99**, (2011).

[18] Y. Berencén, S. Prucnal, F. Liu, I. Skorupa, R. Hübner, L. Rebohle, S. Zhou, H. Schneider, M. Helm, and W. Skorupa, *Room-Temperature Short-Wavelength Infrared Si Photodetector*, Sci. Rep. **7**, (2017).

[19] M. Wang, Y. Berencén, E. García-Hemme, S. Prucnal, R. Hübner, Y. Yuan, C. Xu, L. Rebohle, R. Böttger, R. Heller, H. Schneider, W. Skorupa, M. Helm, and S. Zhou, *Extended Infrared Photoresponse in Te -Hyperdoped Si at Room Temperature*, Phys. Rev. Appl. **10**, (2018).

[20] S. Prucnal, L. Rebohle, and W. Skorupa, *Doping by Flash Lamp Annealing*, Materials Science in Semiconductor Processing.

[21] L. Rebohle, S. Prucnal, and W. Skorupa, *A Review of Thermal Processing in the Subsecond Range: Semiconductors and Beyond*, Semiconductor Science and Technology.

[22] M.-J. Sher, Y.-T. Lin, M. T. Winkler, E. Mazur, C. Pruner, and A. Asenbaum, *Mid-Infrared Absorptance of Silicon Hyperdoped with Chalcogen via Fs-Laser Irradiation*, J. Appl. Phys. **113**, 063520 (2013).

[23] M. Wang, E. García-Hemme, Y. Berencén, R. Hübner, Y. Xie, L. Rebohle, C. Xu, H. Schneider, M. Helm, and S. Zhou, *Silicon-Based Intermediate-Band Infrared Photodetector Realized by Te Hyperdoping*, Adv. Opt. Mater. **9**, (2021).

[24] A. Luque, A. Martí, E. Antolín, and C. Tablero, *Intermediate Bands versus Levels in Non-Radiative Recombination*, Phys. B Condens. Matter **382**, (2006).

[25] H. Castán, E. Pérez, H. García, S. Dueñas, L. Bailón, J. Olea, D. Pastor, E. García-Hemme, M. Irigoyen, and G. González-Díaz, *Experimental Verification of Intermediate Band Formation on Titanium-Implanted Silicon*, J. Appl. Phys. **113**, (2013).

[26] D. Pastor, J. Olea, A. Del Prado, E. García-Hemme, R. García-Hernansanz, and G. González-Díaz, *Insulator to Metallic Transition Due to Intermediate Band Formation in Ti-Implanted Silicon*, Sol. Energy Mater. Sol. Cells **104**, (2012).

[27] M. T. Winkler, D. Recht, M. J. Sher, A. J. Said, E. Mazur, and M. J. Aziz, *Insulator-to-Metal Transition in Sulfur-Doped Silicon*, Phys. Rev. Lett. **106**, (2011).

[28] S. Zhou, F. Liu, S. Prucnal, K. Gao, M. Khalid, C. Baehtz, M. Posselt, W. Skorupa, and M. Helm, *Hyperdoping Silicon with Selenium: Solid vs. Liquid Phase Epitaxy*, Sci. Rep. **5**, (2015).

[29] J. Mathews, A. J. Akey, D. Recht, G. Malladi, H. Efstathiadis, M. J. Aziz, and J. M. Warrender, *On the Limits to Ti Incorporation into Si Using Pulsed Laser Melting*, Appl. Phys. Lett. **104**, (2014).

[30] F. Liu, S. Prucnal, R. Hübner, Y. Yuan, W. Skorupa, M. Helm, and S. Zhou, *Suppressing the Cellular Breakdown in Silicon Supersaturated with Titanium*, J. Phys. D. Appl. Phys. **49**, (2016).

[31] J. Olea, D. Pastor, M. Toledano-Luque, I. Mártil, and G. Gonzlez-Daz, *Depth Profile Study of Ti Implanted Si at Very High Doses*, J. Appl. Phys. **110**, (2011).

[32] J. Narayan, *Interface Instability and Cell Formation in Ion-Implanted and Laser-Annealed Silicon*, J. Appl. Phys. **52**, (1981).

[33] A. J. Akey, D. Recht, J. S. Williams, M. J. Aziz, and T. Buonassisi, *Single-Phase Filamentary Cellular Breakdown Via Laser-Induced Solute Segregation*, Adv. Funct. Mater. **25**, (2015).

[34] J. Olea, M. Toledano-Luque, D. Pastor, E. San-Andrés, I. Mártil, and G. González-Díaz, *High Quality Ti-Implanted Si Layers above the Mott Limit*, J. Appl. Phys. **107**, (2010).

[35] M. Burgelman, P. Nollet, and S. Degrave, *Modelling Polycrystalline Semiconductor Solar Cells*, Thin Solid Films **361**, 527 (2000).

[36] M. J. Aziz, J. Y. Tsao, M. O. Thompson, P. S. Peercy, and C. W. White, *Solute Trapping: Comparison of Theory with Experiment*, Phys. Rev. Lett. **56**, (1986).

[37] K. Iltgen, C. Bendel, A. Benninghoven, and E. Niehuis, *Optimized Time-of-Flight Secondary Ion Mass Spectroscopy Depth Profiling with a Dual Beam Technique*, J. Vac. Sci. Technol. A Vacuum, Surfaces, Film. **15**, 460 (1997).

[38] S. Hocine and D. Mathiot, *Titanium Diffusion in Silicon*, Appl. Phys. Lett. **53**, (1988).

[39] J. Olea, A. del Prado, E. García-Hemme, R. García-Hernansanz, D. Montero, G. González-Díaz, J. Gonzalo, J. Siegel, and E. López, *Strong Subbandgap Photoconductivity in GaP Implanted with Ti*, Prog. Photovoltaics Res. Appl. **26**, (2018).

[40] K. Sánchez, I. Aguilera, P. Palacios, and P. Wahnón, *Assessment through First-Principles Calculations of an Intermediate-Band Photovoltaic Material Based on Ti-Implanted Silicon: Interstitial versus Substitutional Origin*, Phys. Rev. B - Condens. Matter Mater. Phys. **79**, (2009).

[41] M. Fox, *Optical Properties of Solids* (Oxford University Press, 2001).

[42] *See Supplemental Material At*.

[43] F. Urbach, *The Long-Wavelength Edge of Photographic Sensitivity and of the Electronic Absorption of Solids [8]*, Physical Review.

[44] F. Wooten, *OPTICAL PROPERTIES OF SOLIDS* (Academic Press, 1972).

[45] W. Shockley, *The Theory of P-n Junctions in Semiconductors and P-n Junction Transistors*, Bell Syst. Tech. J. **28**, 435 (1949).

[46] S. M. Sze and K. K. Ng, *Physics of Semiconductor Devices* (John Wiley & Sons, Inc., Hoboken, NJ, USA, 2006).

[47] Ş. Altindal, S. Karadeniz, N. Tuğluoğlu, and A. Tataroglu, *The Role of Interface States and Series Resistance on the I-V and C-V Characteristics in Al/SnO2/p-Si Schottky Diodes*, Solid. State. Electron. **47**, 1847 (2003).

[48] T. F. Schulze, L. Korte, E. Conrad, M. Schmidt, and B. Rech, *Electrical Transport Mechanisms in A-Si:H/c-Si Heterojunction Solar Cells*, J. Appl. Phys. **107**, (2010).

[49] H. Matsuura, T. Okuno, H. Okushi, and K. Tanaka, *Electrical Properties of N-Amorphous/p-Crystalline Silicon Heterojunctions*, J. Appl. Phys. **55**, 1012 (1984).

[50] W. Shockley and H. J. Queisser, *Detailed Balance Limit of Efficiency of P-n Junction Solar Cells*, J. Appl. Phys. **32**, 510 (1961).

[51] P. Wurfel, *The Chemical Potential of Radiation*, J. Phys. C Solid State Phys. **15**, 3967 (1982).

[52] S. Wang, *Solid-State Electronics* (McGraw-Hill Book Company, New York, 1966).

[53] S. Q. Lim, C. T.-K. Lew, P. K. Chow, J. M. Warrender, J. S. Williams, and B. C. Johnson, *Process-Induced Defects in Au-Hyperdoped Si Photodiodes*, J. Appl. Phys. **126**, 224502 (2019).

[54] N. M. Johnson, *A Comparison of Ion-Implantation-Induced Deep Levels in Scanned Electron Beam-Annealed and Continuous Wave Laser-Annealed Silicon," in Laser and Electron Beam Processing of Materials* (Elsevier, 1979).

[55] S. Coffa, V. Privitera, F. Priolo, S. Libertino, and G. Mannino, *Depth Profiles of Vacancy- and Interstitial-Type Defects in MeV Implanted Si*, J. Appl. Phys. **81**, 1639 (1998).

[56] D. Pastor, J. Olea, A. Muñoz-Martín, A. Climent-Font, I. Mártil, and G. González-Díaz, *Interstitial Ti for Intermediate Band Formation in Ti-Supersaturated Silicon*, J. Appl. Phys. **112**, (2012).

[57] J. Olea, D. Pastor, E. García-Hemme, R. García-Hernansanz, Á. Del Prado, I. Mártil, and G. González-Díaz, *Low Temperature Intermediate Band Metallic Behavior in Ti Implanted Si*, Thin Solid Films **520**, (2012).

[58] J. R. Morante, J. E. Carceller, P. Cartujo, and J. Barbolla, *Thermal Emission Rates and Capture Cross-Section of Majority Carriers at Titanium Levels in Silicon*, Solid State Electron. **26**, (1983).

[59] T. Roth, M. Rüdiger, W. Warta, and S. W. Glunz, *Electronic Properties of Titanium in Boron-Doped Silicon Analyzed by Temperature-Dependent Photoluminescence and Injection-Dependent Photoconductance Lifetime Spectroscopy*, J. Appl. Phys. **104**, (2008).

[60] W. Shan, W. Walukiewicz, I. J. W. Ager, E. E. Haller, J. F. Geisz, D. J.

Friedman, J. M. Olson, and S. R. Kurtz, *Band Anticrossing in GaInNAs Alloys*, Phys. Rev. Lett. **82**, 1221 (1999).

[61] Y. J. Li, K. M. Yu, G. B. Chen, C. P. Liu, and W. Walukiewicz, *Conduction Band Modifications by d States in Vanadium Doped CdO*, J. Alloys Compd. **822**, 153567 (2020).

[62] A. D. Bristow, N. Rotenberg, and H. M. Van Driel, *Two-Photon Absorption and Kerr Coefficients of Silicon for 850-2200 Nm*, Appl. Phys. Lett. **90**, (2007).

[63] M.-J. Sher, C. B. Simmons, J. J. Krich, A. J. Akey, M. T. Winkler, D. Recht, T. Buonassisi, M. J. Aziz, and A. M. Lindenberg, *Picosecond Carrier Recombination Dynamics in Chalcogen-Hyperdoped Silicon*, Appl. Phys. Lett. **105**, 053905 (2014).

ADDITIONAL INFORMATION:

Supporting Information Contents:

Table S1: Main numerical parameters used for the SCAPS simulation presented in the main text

Figure S1: Spectral dependence of the magnitude $(\boldsymbol{EQE} \times \boldsymbol{h\nu})^{\frac{1}{2}}$ for the temperature range corresponding to the high temperature behaviour. Lines are fits to Eq. 3 in the main text, which allows the identification of the high energy photoresponse edge (E_H).

Figure S2: Spectral dependence of the magnitude $(\boldsymbol{EQE} \times \boldsymbol{h\nu})^{\frac{1}{2}}$ for the temperature range corresponding to the low temperature behaviour. Lines are fits to Eq. 3 in the main text, which allows the identification of the low energy photoresponse edge (E_L) and the high energy photoresponse edge (E_H).

Figure S3: Photodiode current measured as a function of the optical density power for two different wavelengths and temperatures. Both measurements present a linear dependence.

Competing interests: The authors declare no competing financial and non-financial interests.